JGR Space Physics

RESEARCH ARTICLE
10.1029/2022JA030496

Seasonal Variation of Thermospheric Composition Observed by NASA GOLD

Liying Qian[1], Quan Gan[2], Wenbin Wang[1], Xuguang Cai[2], Richard Eastes[2], and Jia Yue[3,4]

[1]High Altitude Observatory, National Center for Atmospheric Research, Boulder, CO, USA, [2]Laboratory for Atmospheric and Space Physics, University of Colorado, Boulder, CO, USA, [3]Goddard Space Flight Center, NASA, Greenbelt, MD, USA, [4]Catholic University of America, Washington, DC, USA

Key Points:

- GOLD $\sum O/N_2$ is compared to $\sum O/N_2$ from GUVI and NRLMSISE-00 on a seasonal time scale, showing consistency
- $\sum O/N_2$ seasonal variation is hemispherically asymmetric with annual/semiannual in the SH but dominant annual in the NH
- The equinox transition of $\sum O/N_2$ highly depends on longitude and latitude

Correspondence to:

L. Qian,
lqian@ucar.edu

Citation:

Qian, L., Gan, Q., Wang, W., Cai, X., Eastes, R., & Yue, J. (2022). Seasonal variation of thermospheric composition observed by NASA GOLD. *Journal of Geophysical Research: Space Physics*, *127*, e2022JA030496. https://doi.org/10.1029/2022JA030496

Received 28 MAR 2022
Accepted 7 JUN 2022

Abstract We examine characteristics of the seasonal variation of thermospheric composition using column number density ratio $\sum O/N_2$ observed by the NASA Global Observations of Limb and Disk (GOLD) mission from low-mid to mid-high latitudes. We also use $\sum O/N_2$ derived from the Global Ultraviolet Imager (GUVI) limb measurements onboard the Thermosphere Ionosphere Mesosphere Energetics and Dynamics (TIMED) satellite and estimated by the NRLMSISE-00 empirical model to aid our investigation. We found that the $\sum O/N_2$ seasonal variation is hemispherically asymmetric: in the southern hemisphere, it exhibits the well-known annual and semiannual pattern, with highs near the equinoxes, and primary and secondary lows near the solstices. In the northern hemisphere, it is dominated by an annual variation, with a minor semiannual component with the highs shifting toward the wintertime. We also found that the durations of the December and June solstice seasons in terms of $\sum O/N_2$ are highly variable with longitude. Our hypothesis is that ion-neutral collisional heating in the equatorial ionization anomaly region, ion drag, and auroral Joule heating play substantial roles in this longitudinal dependency. Finally, the rate of change in $\sum O/N_2$ from one solstice season to the other is dependent on latitude, with more dramatic changes at higher latitudes.

Plain Language Summary We study how the amount of atmosphere constituent in the Earth's thermosphere change over a year at low-mid to mid-high latitudes using the data measured by the We study how the amount of atmosphere constituent in the Earth's thermosphere change over a year at low-mid to mid-high latitudes using the data measured by the NASA Global Observations of Limb and Disk (GOLD) mission. The main constituents in the thermosphere are atomic oxygen (O) and molecular nitrogen (N_2). The ratio of O and N_2, O/N_2, is a common way to measure the relative abundance of these two constituents. The GOLD mission uses instruments aboard on a geostationary satellite to observe O/N_2. We found that how O/N_2 changes over a year is different in the northern and southern hemispheres. In the southern hemisphere, it has an annual and seminal pattern, with high O/N_2 near the equinoxes, and primary and secondary lows near the solstices. In the northern hemisphere, it is mainly an annual pattern, with a minor semiannual component. The semiannual component has high O/N_2 values shifting away from the equinoxes toward the wintertime. We also found that whether O/N_2 is larger in one hemisphere or the other highly depends on longitude.

1. Introduction

Annual and semiannual variations are one of the most prevalent climatological features in both the thermosphere and ionosphere (e.g., Bowman, 2004; Burns et al., 2012; Emmert & Picone, 2010; Pilinski & Crowley, 2015; Qian et al., 2013, 2009; Rishbeth et al., 2000; Zhang et al., 2010, 2005). Paetzold and Zschorner (1961) first reported the annual and semiannual variations in thermosphere mass density through analysis of satellite drag data. They found that global mean mass density in the thermosphere has a primary minimum near the June solstice, a secondary minimum near the December solstice, and maxima near the equinoxes. Bowman (2004) found that the amplitudes and phases of the annual and semiannual variations showed significant changes from year to year and had an altitude dependence.

The Earth is in an elliptical orbit around the Sun. This introduces a ~7% difference in the solar irradiance that reaches the Earth's thermosphere between early July (aphelion) and early January (perihelion), which causes an annual variation in the thermosphere and ionosphere (Zeng et al., 2008). Fuller-Rowell (1998) proposed the "thermospheric spoon" mechanism for global semiannual variation. The summer-to-winter circulation causes

stronger mixing of the thermosphere during the solstices, and thus smaller neutral density scale height and less mass density. Jones et al. (2018) conducted detailed Thermosphere-Ionosphere-Mesosphere Electrodynamics General Circulation Model (TIME-GCM, lower boundary ∼30 km) numerical experiments by changing lower atmosphere gravity wave forcing, tidal forcing, and Earth's obliquity. They found that the "thermospheric spoon" mechanism is the result of the Earth's obliquity.

However, the annual and semiannual variation driven by the sun-earth distance and "thermospheric spoon" is not sufficient to account for the magnitudes of the observed annual and semiannual variation in thermosphere mass density, especially the primary annual low near July (Qian et al., 2009). Qian et al. (2009) found that a seasonally varying eddy diffusion, representing contributions from the lower atmospheric forcing, was needed at the lower boundary of the Thermosphere-Ionosphere-Electrodynamics General Circulation Model (TIE-GCM, lower boundary at ∼97 km) (Qian et al., 2014; Richmond et al., 1992; Roble et al., 1988), to bring the simulated mass density to be in better agreement with satellite drag data. However, since the satellite drag data was a globally averaged dataset, this seasonally varying eddy diffusion was applied globally without considering its potential latitudinal variability. Jones et al. (2017) also found that the TIME-GCM can reproduce the observed global semiannual variation in upper thermospheric density and total electron content, but the global annual variation was weaker than observed. Jones et al. (2021) was able to improve the thermosphere-ionosphere annual and semiannual oscillation in TIE-GCM by imposing climatological lower boundary conditions on O, O_2, and N_2 density in the model. This is a different approach from the one employed by Qian et al. (2009) (imposing seasonally varying eddy diffusion at the lower boundary of TIE-GCM), but with the same goal of trying to account for contributions from the lower atmospheric that are not included in the model.

Lei et al. (2012) examined annual and semiannual variations in thermosphere density observed by Challenging Minisatellite Payload (CHAMP) (Reigber et al., 2002) and Gravity Recovery and Climate Experiment (GRACE) (Tapley et al., 2004) satellites. They found that annual variations become dominant in the southern hemisphere whereas semiannual variations are seen at all latitudes, with amplitudes about 15%–20% of the annual mean.

Yue et al. (2019) analyzed the Global Ultraviolet Imager (GUVI) limb measurements onboard the Thermosphere Ionosphere Mesosphere Energetics and Dynamics (TIMED) satellite and found that the ratio of O and N_2 number density (O/N_2) in the thermosphere shows a strong annual variation at midlatitudes and a clear semiannual variation at lower latitudes. O/N_2, and the column integrated ratio of O and N_2 ($\sum O/N_2$), are a measure of the relative abundance of O and N_2 in the thermosphere. They are often used to represent thermosphere composition.

Mass density measured by CHAMP and GRACE, O/N_2 measured by GUVI limb observations, and $\sum O/N_2$ measured by GUVI disk observations provide annual and semiannual variations at different latitudes, but it is not possible to separate variations due to local time and longitude from the seasonal and latitudinal variations.

Although the annual and semiannual variation was first reported back in the 1960s, we know surprisingly very little about characteristics of these annual and semiannual variations: (a) we are not certain how these annual and semiannual variations vary with latitude, for thermosphere composition, number densities, temperature, and mass density, and ionosphere densities; (b) we know even less about how the annual and semiannual variations vary with longitude, altitude, and local time; (c) to our best knowledge, hardly any studies have been done on how thermosphere composition transitions from one solstice season to the other—the equinox transition; (d) we are not certain about the physical mechanisms of the annual and semiannual variations, especially by the contributions from the lower atmosphere. Because of this, the current representation of the neutral composition and densities and their seasonal variability in the mesosphere and lower thermospheric region in both upper atmosphere and whole atmosphere general circulation models are still far from being accurate.

Much attention has been paid to geomagnetic storm effects on the thermosphere and ionosphere, which is rightly so. However, it has been increasingly recognized that preconditioning (quiet conditions before storms) is important to how the thermosphere and ionosphere respond to geomagnetic storms. Annual and semiannual variations are one of the most prevalent climatological features in both the thermosphere and ionosphere. $\sum O/N_2$, as a measure of the thermospheric composition, is a key parameter for both the thermosphere and ionosphere due to its importance to (a) thermosphere mass density, thus satellite drag determination; (b) ionosphere electron density, thus GPS and HF radio communications. Therefore, the importance of understanding the annual and semiannual variations of $\sum O/N_2$ cannot be overstated.

The NASA Global Observations of Limb and Disk (GOLD) mission has observed the thermosphere and ionosphere in a geostationary orbit from October 2018 to the present. Column integrated ratios $\sum O/N_2$ are derived from daytime disk measurements of O135.6 nm and N_2 Lyman-Birge-Hopfield (LBH) band emission radiance (140.0–150.0 nm). GOLD observes about one third of the Earth's upper atmosphere (~120°W–20°E, 60°N–60°S) simultaneously. The GOLD $\sum O/N_2$ data allow us to study seasonal variations accurately by separating temporal and spatial variations. In this paper, we compare GOLD $\sum O/N_2$ data with $\sum O/N_2$ derived from GUVI disk measurements and estimated using the NRLMSISE-00 empirical model (Picone et al., 2002) for consistency and validation, focusing on the seasonal time scale. We then characterize the latitudinal variability of the seasonal variations of GOLD $\sum O/N_2$ by examining $\sum O/N_2$ at a fixed local time and a fixed longitude.

Section 2 briefly describes GOLD and GUVI $\sum O/N_2$ data; Section 3 presents comparison results and characteristics of the seasonal variations of $\sum O/N_2$ at noon revealed in GOLD data; Section 4 discusses the results; and Section 5 concludes the study.

2. Data

2.1. NASA GOLD $\sum$O/N$_2$ Data

The GOLD instruments are onboard the SES-14 communication satellite, which was launched on 25 January 2018. The SES-14 satellite is in a geostationary orbit over 47.5°W. The GOLD instruments are Far Ultraviolet (FUV) imagers, which consist of two similar and independent channels (Channels A and B) (Eastes et al., 2017, 2020). The GOLD imagers scan a fixed geographic region with a maximum longitude range from 120°W to 20°E and a latitude range from 60°S to 60°N. During the daytime, it observes Earth's airglow emissions from ~134 to 162 nm with a spectral resolution of 0.2 nm. At night, it observes O 135.6 nm emission with a spectral resolution of 0.4 nm. $\sum O/N_2$ referenced at a fixed N_2 column density of 1×10^{17} cm^{-2} is derived from the daytime disk O 135.6 nm and N_2 LBH emission radiance, with a temporal resolution of 30 min (Correira et al., 2021).

Note that the O 135.6 nm emission on the dayside is not purely thermospheric emission because it can also be produced by the radiative recombination of O^+ and thus cause error in derived $\sum O/N_2$, which may not be negligible, especially at the crest of the equatorial ionization anomaly (EIA). Correira et al. (2021) estimated that the error in the derived GOLD $\sum O/N_2$ due to radiative recombination of O^+ is ~1%–2% for a wide range of solar zenith and emission angles during periods of low solar and geomagnetic activity (the first few years of the GOLD mission), but the error will become larger as geomagnetic activity increases during Solar Cycle 25, with a potential of reaching ~ 10%–20%. In addition, sometimes GOLD $\sum O/N_2$ in the equatorial region is uncharacteristically large (Figure 1a). This is an artifact introduced when the current flat-field correction is unable to correctly compensate for detector degradation where the aurora and the high-latitude, sunlit limb—which is also seen during night side observations near solstices, are observed. As a result, we avoid the equatorial region and examine the seasonal variations in the latitude region from 20° to 60° (low-mid to mid-high latitudes) in this study. In addition, for the version 3 data used in this study, a linear trend of −7% per year in the $\sum O/N_2$ has been identified. This decrease is attributed to the flat-field correction used to remove date dependent, spatial variations in sensitivity. We remove this linear trend in the GOLD $\sum O/N_2$ when we study the characteristics of seasonal variations (Figure 2). A more robust flat-field correction has been developed and will be used for the next data update. GOLD $\sum O/N_2$ are available online at http://gold.cs.ucf.edu/search/.

2.2. NASA TIMED/GUVI $\sum$O/N$_2$ Data

The TIMED satellite was launched on 7 December 2001. The GUVI instrument aboard the satellite provides images and spectra of FUV emissions from the thermosphere in the wavelengths between 115 and 180 nm on both dayside and nightside (Christensen et al., 2003; Paxton et al., 1999). The GUVI disk dayglow data at O 135.6 nm and N_2 LBH (140–150 nm) have been used to derive $\sum O/N_2$ referenced at a fixed N_2 column density of 1×10^{17} cm^{-2} (Zhang et al., 2004). GUVI $\sum O/N_2$ are available at: http://guvitimed.jhuapl.edu/data_products.

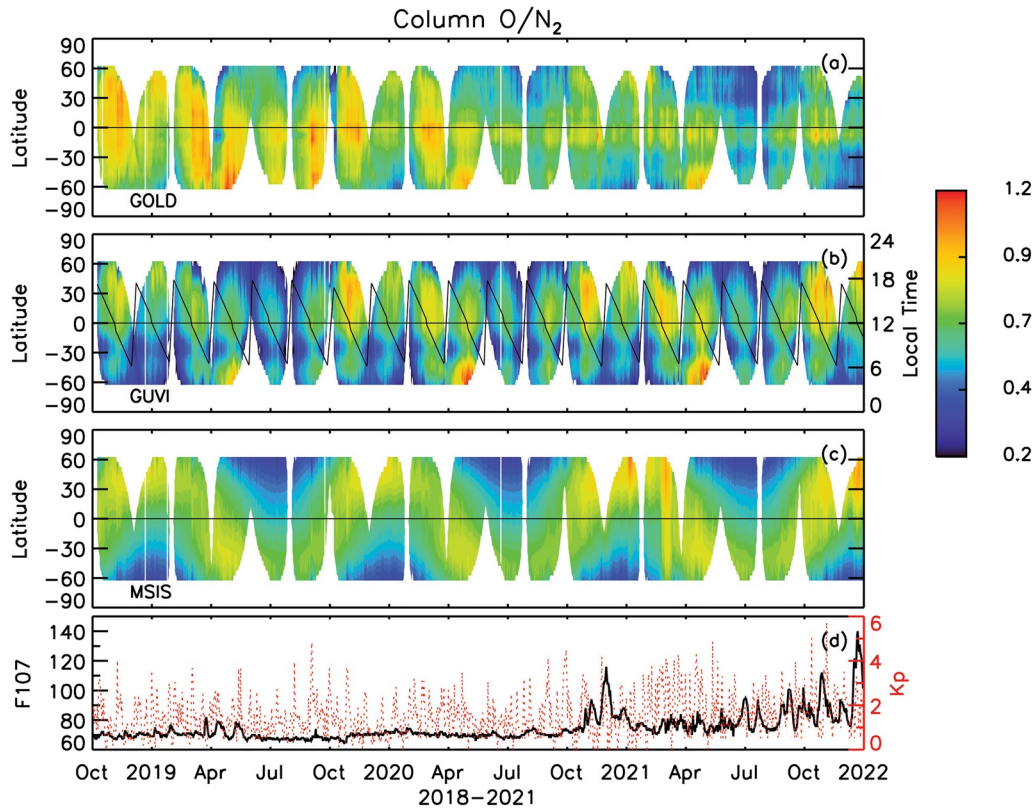

Figure 1. Comparisons of $\sum O/N_2$ from GOLD, GUVI, and NRLMSISE-00 at the conjunction of the GOLD FOV and GUVI orbits from October 2019 to the end of 2021. (a) GOLD; (b) GUVI; (c) NRLMSISE-00; (d) *F10.7* (black line) and *Kp* (red line) indices. The local times shown in (b) are the GUVI sampling local times.

3. Results

We first compare $\sum O/N_2$ from GOLD, GUVI, and NRLMSISE-00, focusing on the seasonal time scale. As mentioned earlier, GOLD is on a geosynchronous orbit whereas TIME/GUVI is on a high-inclination, low-Earth orbit. To conduct meaningful comparisons, we obtain $\sum O/N_2$ from GOLD, GUVI, and NRLMSISE-00 at the intersection of the GOLD field of view (FOV) and GUVI orbits: (a) run NRLMSISE-00 globally using a resolution of 5° latitude by 5° longitude by 2 km, in the altitude range of 100–450 km, with a time step of one hour; (b) for each 5° latitude bin, obtain $\sum O/N_2$ observed concurrently by GOLD and GUVI at the intersection of the GOLD FOV and GUVI orbits for each day, and then calculate daily mean $\sum O/N_2$; (c) calculate the corresponding NRLMSISE-00 daily mean $\sum O/N_2$ at the intersection of the GOLD FOV and GUVI orbits.

Figures 1a–c are the daily mean $\sum O/N_2$ obtained from GOLD, GUVI, and NRLMSISE-00, respectively, in the latitude range of 60°S–60°N, from October 2018 to the end of 2021. The zig-zag black line in Figure 1b shows the GUVI observation local times, which are also the local times for the GOLD and NRLMSISE-00 $\sum O/N_2$ in Figures 1a and 1c. Figure 1d shows the *F10.7* (black) and *Kp* (red) indices for this period. Daily *F10.7* and daily *Ap* were used as input for NRLMSISE-00. Daily *Kp* is plotted in Figure 1d to show small geomagnetic variations from October 2018 to October 2021 more clearly (*Ap* is proportional to the exponential of *Kp*). Note that $\sum O/N_2$ from GOLD is systematically higher than NRLMSISE-00, whereas $\sum O/N_2$ from GUVI is systematically lower than NRLMSISE-00. GOLD $\sum O/N_2$ in Figure 1a was therefore divided by 1.25 and GUVI $\sum O/N_2$ in Figure 1b was multiplied by 1.25 for comparison purposes. It is not clear what caused this systematic difference among the datasets. One possible reason is the difference in the altitude registration among GOLD, GUVI, and NRLMSISE-00 to where the N_2 column number density is 1×1.0^{17} cm^{-2}. This systematic difference is likely less of a concern when the focus is on seasonal variability.

Note that GUVI $\sum O/N_2$ is low in the latitude range ~10°S–40°S. This is an artifact due to impact of energetic particles (>1 Mev) from the Southern Atlantic Anomaly (SAA) on the GUVI instruments.

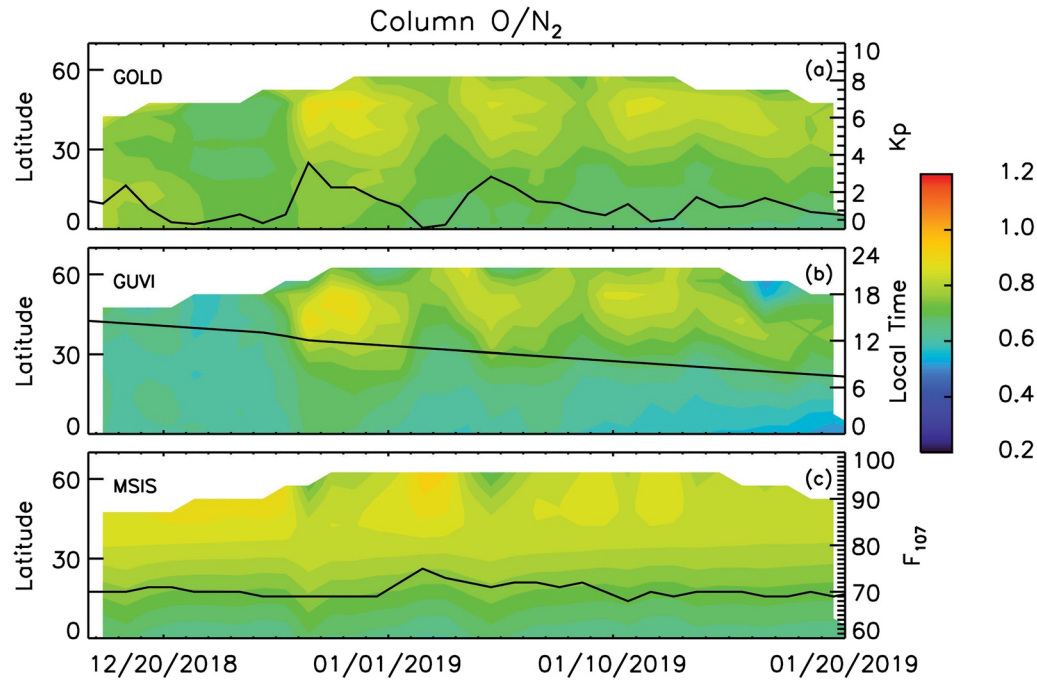

Figure 2. A zoom-in to the period from 12/18/2018 to 01/20/2019 in Figure 1 to show multi-day variations. (a) GOLD observation; (b) GUVI observation; (c) corresponding NRLMSISE-00 calculations. *Kp*, local time, and *F10.7* are overplotted in (a), (b), (c), respectively.

A predominant annual variation with a summer low and winter high in $\sum O/N_2$ at higher latitudes (greater than ~ 30°) is a consistent feature in all three datasets. The winter high $\sum O/N_2$ at higher latitudes in one hemisphere transitions to the winter high at higher latitudes in the other hemisphere through the equinoxes and the lower latitudes, giving rise to seasonal variations at different latitudes with different annual and semiannual components. These overall seasonal/latitudinal patterns of $\sum O/N_2$ are consistent in the three datasets.

An interesting feature is that multi-day variations consistent with geomagnetic forcing (Qian & Solomon, 2011), shown as shorter-term variability in Figures 1a and 1ure 1b, are evident in both GOLD and GUVI datasets. The multi-day variation is not a focus of this study, but it is useful to zoom in on Figure 1 to see how well $\sum O/N_2$ from GOLD, GUVI, and NRLMSISE-00 compare in this shorter time scale for validation purpose. Figure 2 shows a ~ 1-month period from 12/18/2018 to 1/20/2019 taken from Figure 1. *Kp*, local time, and *F10.7* are overplotted in Figures 2a–2c respectively. There is a very good correspondence between the $\sum O/N_2$ from GOLD and from GUVI, and between the $\sum O/N_2$ and the *Kp* index, except for during the small increase of *Kp* before 12/20/2018 when there is a clear response in the GOLD data but not much in the GUVI data. The correspondence between the *Kp* and $\sum O/N_2$ from NRLMSISE-00 is not as good compared to those for GOLD and GUVI. NRLMSISE-00 uses empirical parameterization to estimate geomagnetic forcing effects, so it is difficult to accurately represent effects of a specific geomagnetic disturbance.

We now examine the latitudinal variability of the seasonal variations of GOLD $\sum O/N_2$ at a fixed local time and a fixed longitude. Note that for a fixed solar zenith angle (SZA) along the GOLD line-of-sight, which is valid for SZAs less than ~80°, the intensity ratio of O 135.6 nm and N2 LBH is constant to within a few percent for emission angles less than 40°. For emission angles greater than 60° the maximum systematic error is ~10% for large values of $\sum O/N_2$ (Correira et al., 2021). The subsatellite longitude of GOLD is at 47.5°W. Therefore, we focus on examining the seasonal variation of $\sum O/N_2$ at 45°W and local noon. This can keep the systematic error due to emission angles lower. Figure 3 shows the seasonal variations at 45°W and 12:00 LT, at four latitudes in each hemisphere: 52.5°N (green), 42.5°N (brown), 32.5°N (red), and 22.5°N (blue) in Figure 3a, and 52.5S (green), 42.5°S (brown), 32.5°S (red), and 22.5°S (blue) in Figure 3b. We also calculate the $\sum O/N_2$ difference between a northern hemisphere latitude and its corresponding southern hemisphere latitude. Figure 3c shows the $\sum O/N_2$ differences between pairs of northern and southern latitudes at 52.5° (green), 42.5° (brown), 32.5° (red), and

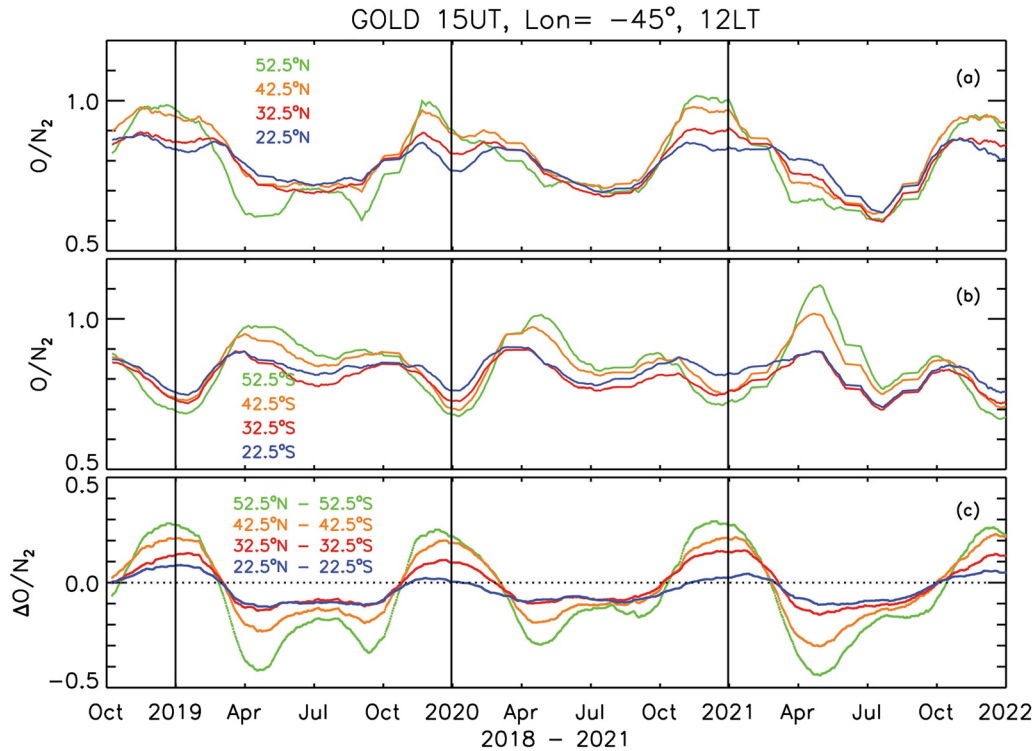

Figure 3. Seasonal variations of $\sum O/N_2$ at noon and 45°W from October 2019 to the end of 2021, observed by GOLD: (a) time series of $\sum O/N_2$ at 52.5°N (green), 42.5°N (brown), 32.5°N (red), 22.5°N (green); (b) time series of $\sum O/N_2$ at 52.5°S (green), 42.5°S (brown), 32.5°Sc (red), 22.5°S (green); (c) time series of $\sum O/N_2$ differences between pairs of northern hemisphere latitudes and the corresponding southern hemisphere latitudes. Green: 52.5°; brown: 42.5°; red: 32.5°; blue: 22.5°.

22.5° (blue). We define the time period when the $\sum O/N_2$ difference is positive as *the December solstice season*, the period when it is negative as *the June solstice season*, and the transition between the two as *the equinox transition*. The vertical black lines in Figure 3 show the beginning of years 2019, 2020, and 2021. Note that in Figures 3–6, we use $\sum O/N_2$ from GOLD and NRLMSISE-00 without applying a scaling factor.

There are three distinct characteristics in the seasonal variations:

1. There is a clear hemispheric asymmetry in the seasonal variations. In the southern hemisphere, the seasonal variations exhibit the well-known annual and semiannual pattern, with the highs near the equinoxes, and primary and secondary lows near the solstices. The March equinox highs occur earlier at lower latitudes than at higher latitudes, whereas the September equinox highs occur earlier at higher latitudes than at lower latitudes. In the northern hemisphere, however, the seasonal pattern is dominated by an annual variation. There is a small semiannual component, but the highs of the semiannual component shift earlier in the case of the March equinox and shift later in the case of the September equinox, toward the wintertime, with a larger shift at higher latitudes. In both hemispheres, the annual and semiannual amplitudes increase with latitude.
2. The December solstice season is much shorter than the June solstice season (Figure 3c). The average durations for the December solstice season and the June solstice season during this period (October 2018–the end of 2021) are 122 and 243 days, respectively.
3. The $\sum O/N_2$ difference in Figure 3c increases as latitude increases in both the December and June solstice seasons, but the transition times between the two solstice seasons, that is, the timing of the equinox transition, do not change much with latitudes except at 22.5° when the $\sum O/N_2$ difference is very small.

We further examine whether these characteristics of the seasonal variations from GOLD $\sum O/N_2$ are present in the corresponding NRLMSISE-00 $\sum O/N_2$. Note that the local time of GUVI $\sum O/N_2$ varies from day-to-day due to

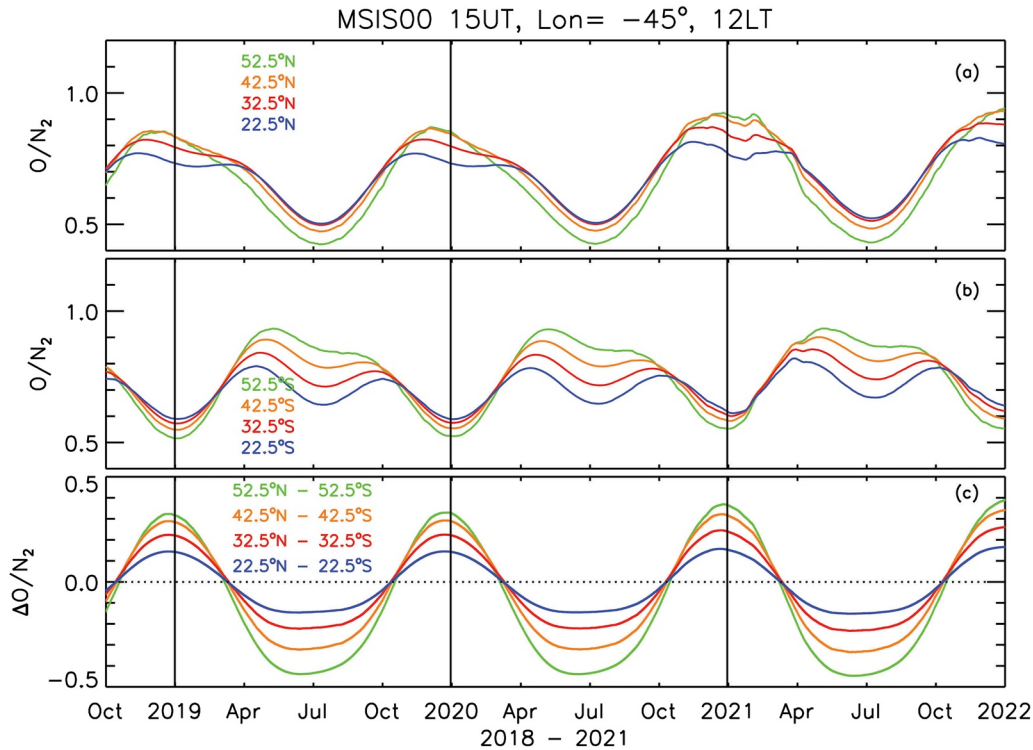

Figure 4. Seasonal variations of $\sum O/N_2$ at noon and 45°W from October 2019 to the end of 2021, calculated by NRLMSISE-00: (a) time series of $\sum O/N_2$ at 52.5°N (green), 42.5°N (brown), 32.5°N (red), 22.5°N (green); (b) time series of $\sum O/N_2$ at 52.5°S (green), 42.5°S (brown), 32.5°S (red), 22.5°S (green); (c) time series of $\sum O/N_2$ differences between pairs of northern hemisphere latitudes and the corresponding southern hemisphere latitudes. Green: 52.5°; brown: 42.5°; red: 32.5°; blue: 22.5°.

orbital precession, and the longitudes of GUVI $\sum O/N_2$ change from orbit to orbit on each day, so GUVI $\sum O/N_2$ is not used here. Figure 4 is the same as Figure 3 except that the results are from NRLMSISE-00.

NRLMSISE-00 $\sum O/N_2$ shows seasonal characteristics that are consistent with those shown in GOLD $\sum O/N_2$:

1. There is a hemispheric asymmetry in the seasonal variations of NRLMSISE-00 $\sum O/N_2$ that is consistent with that in GOLD $\sum O/N_2$.
2. The December solstice season for NRLMSISE-00 $\sum O/N_2$ is also much shorter than the June solstice season. The average durations for the December and June solstice seasons during this data period are 145 and 220 days, respectively.
3. The $\sum O/N_2$ differences in Figure 4c also increases as latitude increases in both the December and June solstice seasons, and the transition times between the two solstice seasons also do not change much with latitude.

The December solstice season is shorter in duration than the June solstice season at all latitudes in both GOLD and NRLMSISE-00 $\sum O/N_2$ (Figures 3c and 4c). To find out whether the hemispheric asymmetry and this duration difference between the December and June solstice seasons are global phenomena, we analyze the NRLMSISE-00 results at 135°E. Note that 135°E is chosen to represent an east longitude sector that contrasts the west longitude sector that 45°W represents. Also note that we use NRLMSISE-00 $\sum O/N_2$ since 135°E is not in the GOLD field of view. Figure 5 is the same as Figure 4 except that the results are for 135°E. We notice that the hemispheric asymmetry in the seasonal variations at 135°E is consistent with the results at 45°W, with well-defined annual and semiannual variations in the southern hemisphere but dominant annual variations in the northern hemisphere. However, there are two significantly different aspects between the results at 135°E and 45°W:

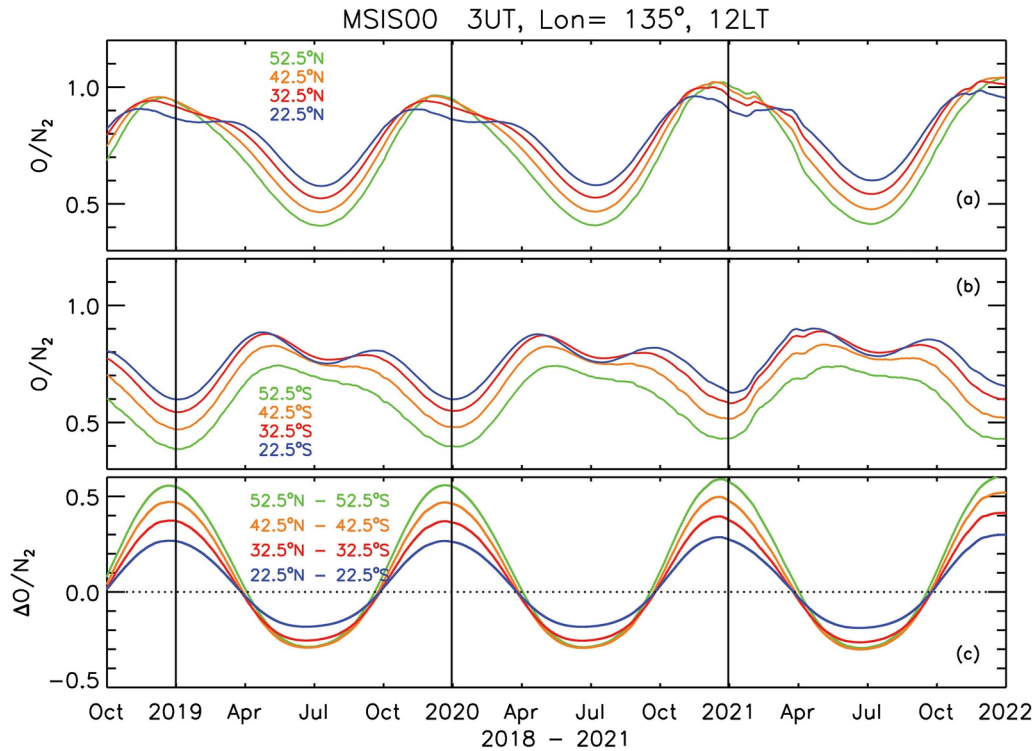

Figure 5. Seasonal variations of $\sum O/N_2$ at noon and 135°E from October 2019 to the end of 2021, calculated by NRLMSISE-00: (a) time series of $\sum O/N_2$ at 52.5°N (green), 42.5°N (brown), 32.5°N (red), 22.5°N (green); (b) time series of $\sum O/N_2$ at 52.5°S (green), 42.5°S (brown), 32.5°Sc (red), 22.5°S (green); (c) time series of $\sum O/N_2$ differences between pairs of northern hemisphere latitudes and the corresponding southern hemisphere latitudes. Green: 52.5°; brown: 42.5°; red: 32.5°; blue: 22.5°.

1. There is significant difference in the latitudinal variation of $\sum O/N_2$ in the southern hemisphere between the results at 135°E and 45°W. During the June solstice season, $\sum O/N_2$ increases with latitude at 45°W; at 135°E, the largest $\sum O/N_2$ is at 32.5°S, with O/N_2 decreasing with latitude from 32.5°S to 52.5°S.
2. Compared to the results at 45°W, the duration of the December solstice season (187 days) at 135°E has increased significantly and become longer than the June solstice season (178 days); the magnitudes of the O/N_2 differences have also switched between the December and June solstice seasons compared to the ones at 45°W (Figures 4c and 5c).

These differences demonstrate that the latitude region of the winter high $\sum O/N_2$, the durations of the June and December solstice seasons, and the magnitudes of the hemispheric $\sum O/N_2$ difference, are all highly dependent on longitude, presumably due to a longitudinal dependence in the seasonal variation forcing.

Figure 6 show the 3-year average $\sum O/N_2$ (2019, 2020, and 2021) for GOLD at (45°W, 12LT), NRLMSISE-00 at (45°W, 12LT), and NRLMSISE-00 at (135°E, 12LT) for easier comparisons. It summarizes the hemispheric asymmetry of the seasonal variations of $\sum O/N_2$ and the latitudinal and longitudinal dependences of the timing of the equinox transition of $\sum O/N_2$ we described earlier.

4. Discussion

4.1. Hemispheric Asymmetry

Figure 6 of Yue et al. (2019) shows GUVI limb O/N_2 in the lower (8.4×10^{-4} Pa, ~130 km) and upper (6.35×10^{-6} Pa, ~300 km) thermosphere in five latitude zones (30°–60°N, 10°–30°N, 10°S to 10°N, 30°–10°S, and 60°–30°S). In both the lower and upper thermosphere, O/N_2 in the latitude zones 10°–30°N and 30°–10°S

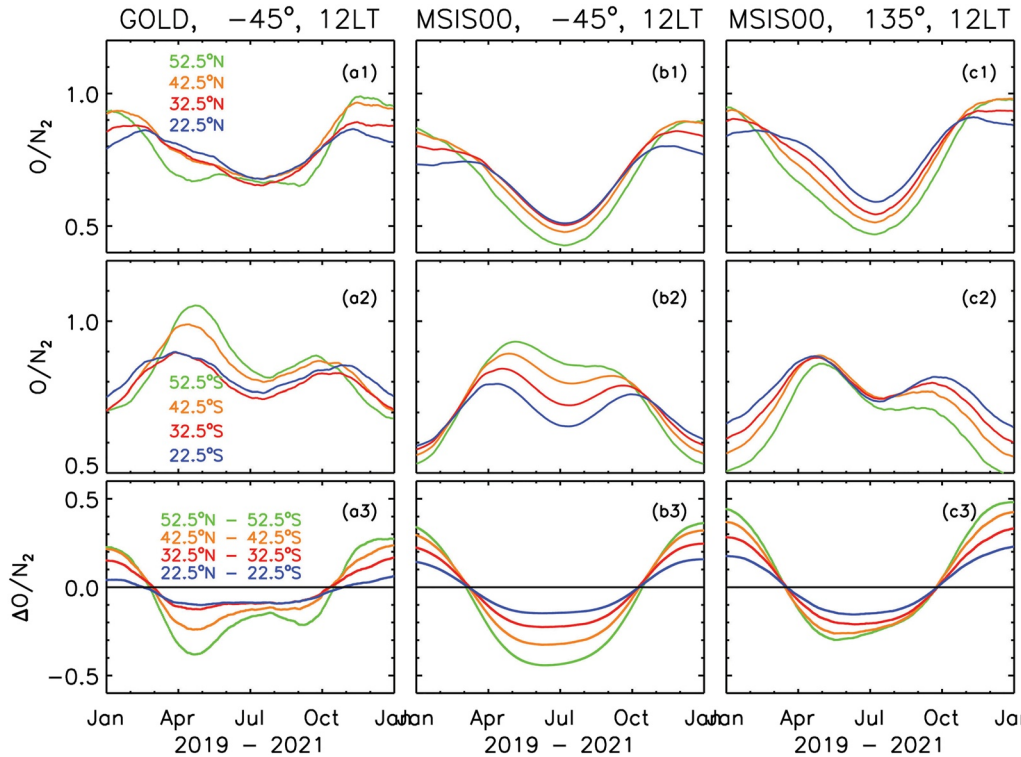

Figure 6. 3-year average $\sum O/N_2$ (2019, 2020, and 2021) for GOLD at (45°W, 12LT), NRLMSISE-00 at (45°W, 12LT), and NRLMSISE-00 at (135°E, 12LT). (a1, b1, c1) time series of $\sum O/N_2$ at 52.5°N (green), 42.5°N (brown), 32.5°N (red), 22.5°N (green); (a2, b2, c2) time series of $\sum O/N_2$ at 52.5°S (green), 42.5°S (brown), 32.5°Sc (red), 22.5°S (green); (a3, b3, c3) time series of $\sum O/N_2$ differences between pairs of northern hemisphere latitudes and the corresponding southern hemisphere latitudes. Green: 52.5°; brown: 42.5°; red: 32.5°; blue: 22.5°.

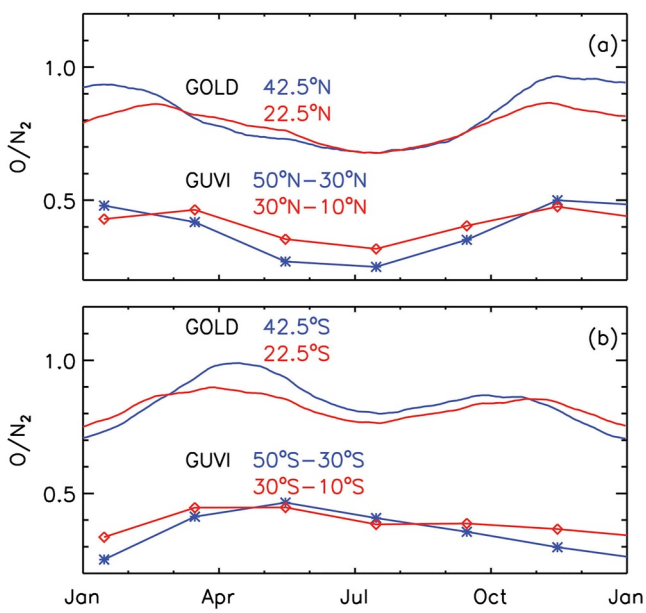

Figure 7. (a) GOLD 3-year average $\sum O/N_2$ for 42.5°N and 22.5°N from Figure 6, and GUVI 3-year average O/N_2 (2004, 2005, 2006) at 8.4×10^{-4} Pa (~130 km) in the latitude bins of 50°N–30°N and 30°N–10°N based on Figure 6 of Yue et al. (2019); (b) the corresponding results in the southern hemisphere.

exhibit a hemispheric asymmetry similar to the hemispheric asymmetry in the GOLD and NRLMSISE-00 $\sum O/N_2$: at 30°–10°S, the highs of the semiannual component is near the equinoxes; at 10°–30°N, the highs of the semiannual component shift more toward the wintertime, although it is difficult to discern whether the annual component is more dominant. In both the lower and upper thermosphere, the seasonal variation of O/N_2 in the latitude zones 30°–60°N and 60°–30°S are dominated by an annual variation, with only a remnant semiannual component. It is difficult to discern the semiannual component at 60°–30°S, but at 30°–60°N, a semiannual component is evident in 2006. The high O/N_2 of this northern hemisphere semiannual component also shifts away from the equinoxes toward the wintertime, consistent with those in GOLD $\sum O/N_2$. Note that in GOLD, the northern hemisphere is also dominated by an annual variation, but the southern hemisphere has clear annual and semiannual variations in this latitude region. Note also that these density ratio O/N_2 values are not $\sum O/N_2$ as in the case of GOLD, but both Yue et al. (2019) and Yu et al. (2020) found that the annual and semiannual variations in composition have a constant phase with altitude throughout the thermosphere. Figure 7a shows GOLD 3-year average $\sum O/N_2$ (2019, 2020, and 2021) for 42.5°N and 22.5°N from Figure 6 of this paper, and GUVI 3-year average O/N_2 (2004, 2005, and 2006) at 8.4×10^{-4} Pa (~130 km) in the latitude bins of 50°N–30°N and 30°N–10°N based on Figure 6 of Yue et al. (2019), whereas Figure 7b shows the corresponding results in the southern hemisphere. Note that the years (and therefore solar EUV radiation level), the latitudes, the local times are all different between the GOLD and GUVI

results. In addition, GOLD $\sum O/N_2$ are column density ratios, which are heavily weighted by O/N_2 in the altitude region of ~140–180 km, whereas GUVI O/N_2 is at ~130 km. Consequently, there are evident differences between the GOLD and GUVI results in Figure 7, for example, their magnitudes and seasonal amplitudes, but it is difficult and can be misleading to try to interpret these differences. Therefore, Figure 7 is shown for reference only. Note also that the GUVI O/N_2 has six data points for each year (each data point is a 2-month average, see Yue et al., 2019 for details), whereas the GOLD $\sum O/N_2$ has a daily temporal resolution. Consequently, the GOLD $\sum O/N_2$ shows more details in its seasonal pattern, and it is easier to discern the hemispheric asymmetry in the thermospheric composition.

4.2. Longitudinal Dependency of the Equinox Transition

We know that near the solstices, $\sum O/N_2$ is high in the winter hemisphere, and low in the summer hemisphere. Then questions arise as to how does this summer-to-winter latitudinal distribution of $\sum O/N_2$ transition from one solstice season to the other through the equinoxes? Will there be a period near the two equinoxes when $\sum O/N_2$ is distributed approximately evenly around the equator? If there is such a period, then how long is it? Figures 3c, 4c and 5c shows that there is no evident period around the equinoxes, or "equinox season", when the composition of pairs of the northern and southern latitudes in the latitude region of 20°–60° is approximately the same. $\sum O/N_2$ is either higher in one hemisphere or the other. Therefore, as far as $\sum O/\mathrm{N}_2$ is concerned, there is only the December solstice season or June solstice season, and the transition between the December solstice and June solstice seasons, *the equinox transition*, has a time scale on the order of 1 day since the data temporal resolution is 1 day in these figures. The timings of the equinox transition, which determine the durations of the December solstice and June solstice seasons, are highly variable with longitude. In addition, the magnitudes of the hemispheric $\sum O/N_2$ differences, and the winter downwelling zone of the summer-to-winter circulation, which determines where $\sum O/N_2$ maximizes, are also longitudinally dependent.

Rishbeth and Müller-Wodarg (1999) found that the latitude of the downwelling regions varies with longitude because the thermospheric circulation is influenced by the high-latitude energy inputs, which are related to the geometry of the Earth's magnetic field. Qian, Burns, Wang, Solomon, Zhang, et al. (2016) found that the latitude of the downwelling regions also varies with longitude because of the ion-neutral collisional heating in the EIA region and ion drag. The longitudinal dependencies in the EIA ion-neutral collisional heating, ion drag, and auroral Joule heating result in a strong longitudinal variation of $\sum O/N_2$ derived from GUVI disk observations (Qian, Burns, Wang, Solomon, & Zhang, 2016). Our hypothesis is that the EIA ion-neutral collisional heating, ion drag, and auroral Joule heating play substantial roles in determining the longitudinal dependency of the durations of the June and December solstice seasons and the magnitudes of the $\sum O/N_2$ differences during the two solstice seasons. Further studies are needed to fully uncover the physical processes by which this dependence occurs.

Note that the results shown in Figures 4 and 5 are at a fixed local time (local noon) at different longitudes (45°W and 135°E), so they are from different universal times (UTs, 15UT and 3UT, respectively). Therefore, the difference between results in Figures 4 and 5 are not entirely longitudinal variations. It also includes effects of the UT variation. As the UT changes and the magnetic poles rotate around the geographic pole, the auroral Joule heating in both the hemispheres varies. Weimer et al. (2020) found that this UT variation of auroral Joule heating can cause substantial variations in exosphere temperatures, especially in the polar regions: the maximum exosphere temperature occurred in the Southern polar region around 9 UT, in the Northern polar region at 21 UT, while the two poles are roughly equal at 3 UT and 15 UT. In this paper, 15 UT (Figure 4) and 3 UT (Figure 5) were chosen to minimize the UT effects and to underscore the longitudinal variations.

4.3. Latitudinal Dependency of the Equinox Transition

Whether during the December or June solstice seasons, the hemispheric $\sum O/N_2$ differences increase with latitude, but the transition times between the two solstice seasons, the timings of the equinox transition, do not change much with latitude. This indicates that the rate of change in composition from one solstice season to the other is more dramatic at higher latitudes. Therefore, this aspect of the equinox transition is highly dependent on latitude.

Since upwelling decreases $\sum O/N_2$ and downwelling increases $\sum O/N_2$, we can understand this latitudinal dependency by following the thermospheric circulation. On a daily average basis, the summer polar region has the

largest solar heating (TIE-GCM model calculation, not shown), so upwelling is the largest, which causes a larger decrease of $\sum O/N_2$ at higher latitudes than at lower latitudes. This high latitude upwelling is further enhanced by the auroral Joule heating, which is present even at geomagnetically quiet periods (Cai et al., 2020, 2021). As the meridional wind encounters the EIA, it is suppressed in the summer hemisphere but accelerates after it passes the EIA in the winter hemisphere (Qian, Burns, Wang, Solomon, Zhang, et al., 2016). The wind then converges due to auroral Joule heating, producing large $\sum O/N_2$ at subauroral latitudes.

The lower atmosphere can also contribute to the latitudinal dependency of the summer-to-winter difference in $\sum O/N_2$. Seasonal and latitudinal variations in wave/tidal activity, turbulent mixing, and residual circulations in the mesosphere and lower thermosphere region strongly impact the seasonal and latitudinal variations of thermosphere composition (e.g., Jones et al., 2017, 2014; Wu et al., 2017; Yamazaki & Richmond, 2013). For example, the lower thermospheric residual circulation reduces the summer-to-winter gradient of O/N_2 (Qian & Yue, 2017).

Note that GOLD $\sum O/N_2$ shows a double low feature at mid to mid-high latitudes in the northern hemisphere during the June solstice season (52.5°N in Figure 3a for 2019, 42.5° and 52.5° in Figure 3c for 2019, 2020, and 2021). NRLMSISE-00 $\sum O/N_2$ does not have this double low feature (Figures 4 and 5). More observations and modeling work are needed to determine the nature of this double low feature.

5. Conclusions

We compare GOLD $\sum O/N_2$ with $\sum O/N_2$ from GUVI disk observations and NRLMSISE-00 for consistency focusing on the seasonal time scale. We further characterize the latitudinal variability of the seasonal variation from low-mid to mid-high latitudes at a fixed local time and a fixed longitude using $\sum O/N_2$ from GOLD and NRLMSISE-00.

We found that the overall seasonal/latitudinal patterns of $\sum O/N_2$ in the GOLD, GUVI, and NRLMSISE-00 are consistent: an annual variation with a summer low and a winter high in $\sum O/N_2$ at higher latitudes. The winter high $\sum O/N_2$ at higher latitudes in one hemisphere transitions to winter high at higher latitudes in the other hemisphere through the equinoxes and lower latitudes, yielding seasonal variations at different latitudes with different annual and semiannual components.

There is a hemispheric asymmetry in the seasonal variation patterns: in the southern hemisphere, the seasonal variations exhibit the well-known annual and semiannual pattern, with highs near the equinoxes, and primary and secondary lows near the solstices. In the northern hemisphere, the seasonal pattern is dominated by an annual variation, with a minor semiannual component with the highs shifting away from the equinoxes toward the wintertime.

In addition, as demonstrated by the results from NRLMSISE-00, the characteristics associated with the equinox transition, including the durations of the December and June solstice seasons, the magnitudes of the $\sum O/N_2$ differences between the two hemispheres, and the downwelling convergence latitudes, are highly variable with longitude. Our hypothesis is that the EIA ion-neutral collisional heating, ion drag, and auroral Joule heating play substantial roles in determining the longitudinal dependence of these characteristics.

Finally, the rate of change in $\sum O/N_2$ from one solstice season to the other is more dramatic at higher latitudes. Therefore, the equinox transition is also highly dependent on latitude.

Future work involves using numerical model simulations to investigate physical mechanisms of the hemispheric asymmetry in the seasonal variation patterns, and the longitudinal and latitudinal dependencies of the equinox transitions.

Data Availability Statement

GOLD $\sum O/N_2$ are available online at http://gold.cs.ucf.edu/search/. GUVI $\sum O/N_2$ are available at: http://guvitimed.jhuapl.edu/data_products. The data used to produce the figures in this paper are available at https://doi.org/10.5065/p3wa-1q97.

Acknowledgments
This study is supported by NASA grants 80NSSC20K0189, 80NSSC19K0278, 80NSSC18K0648, NNH19ZDA001N-HGIO, 80NSSC19K0835, NNH19ZDA001N-HSR, NNH19ZDA001N-HTMS and 80NSSC21K1315. This study is also supported by NASA contract 80GSFC18C0061 to the University of Colorado. The National Center for Atmospheric Research is a major facility sponsored by the National Science Foundation under Cooperative Agreement No. 1852977.

References

Bowman, B. R. (2004). *The semiannual thermosphere density variation from 1970 to 2002 between 200-1100km, AAS 2004-174, AAS/AIAA spaceflight Mechanics Meeting, Maui, Hi, February. Davies, K. (1990)*. Ionospheric Radio, Peter Peregrinus.

Burns, A. G., Solomon, S. C., Wang, W., Qian, L., Zhang, Y., & Paxton, L. J. (2012). Daytime climatology of ionospheric NmF2 and hmF2 from COSMIC data. *Journal of Geophysical Research*, *117*, A09315. https://doi.org/10.1029/2012JA017529

Cai, X., Burns, A. G., Wang, W., Qian, L., Pedatella, N., Coster, A., et al. (2021). Variations in thermosphere composition and ionosphere total electron content under "geomagnetically quiet" conditions at solar-minimum. *Geophysical Research Letters*, *48*, e2021GL093300. https://doi.org/10.1029/2021gl093300

Cai, X., Burns, A. G., Wang, W., Qian, L., Solomon, S. C., Eastes, R. W., et al. (2020). The two-dimensional evolution of thermospheric ΣO/N2 response to weak geomagnetic activity during solar-minimum observed by GOLD. *Geophysical Research Letters*, *47*, e2020GL088838. https://doi.org/10.1029/2020gl088838

Christensen, A. B., Paxton, L. J., Avery, S., Craven, J., Crowley, G., Humm, D. C., et al. (2003). Initial observations with the global ultraviolet imager (GUVI) in the NASA TIMED satellite mission. *Journal of Geophysical Research*, *108*(A12), 1451. https://doi.org/10.1029/2003JA009918

Correira, J., Evans, J. S., Lumpe, J. D., Krywonos, A., Daniell, R., Veibell, V., et al. (2021). Thermospheric composition and solar EUV flux from the Global-scale Observations of the Limb and Disk (GOLD) mission. *Journal of Geophysical Research: Space Physics*, *126*, e2021JA029517. https://doi.org/10.1029/2021ja029517

Eastes, R. W., McClintock, W. E., Burns, A. G., Anderson, D. N., Andersson, L., Aryal, S., et al. (2020). Initial observations by the global-scale observations of the limb and disk (GOLD) mission. *Journal of Geophysical Research: Space Physics*, *125*, e2020JA027823. https://doi.org/10.1029/2020JA027823

Eastes, R. W., McClintock, W. E., Burns, A. G., Anderson, D. N., Andersson, L., Codrescu, M., et al. (2017). The global-scale observations of the limb and disk (GOLD) mission. *Space Science Reviews*, *212*(1–2), 383–408. https://doi.org/10.1007/s11214-017-0392-2

Emmert, J. T., & Picone, J. M. (2010). Climatology of globally averaged thermospheric mass density. *Journal of Geophysical Research*, *115*, A09326. https://doi.org/10.1029/2010JA015298

Fuller-Rowell, T. J. (1998). The "thermospheric spoon": A mechanism for the semiannual density variation. *Journal of Geophysical Research*, *103*, 3951–3956. https://doi.org/10.1029/97ja03335

Jones, M., Emmert, J. T., Drob, D. P., Picone, J. M., & Meier, R. R. (2018). Origins of the thermosphere-ionosphere semiannual oscillation: Reformulating the "thermospheric spoon" mechanism. *Journal of Geophysical Research: Space Physics*, *123*, 931–954. https://doi.org/10.1002/2017JA024861

Jones, M., Emmert, J. T., Drob, D. P., & Siskind, D. E. (2017). Middle atmosphere dynamical sources of the semiannual oscillation in the thermosphere and ionosphere. *Geophysical Research Letters*, *44*, 12–21. https://doi.org/10.1002/2016gl071741

Jones, M., Jr., Forbes, J. M., & Hagan, M. E. (2014). Tidal-induced net transport effects on the oxygen distribution in the thermosphere. *Geophysical Research Letters*, *41*, 5272–5279. https://doi.org/10.1002/2014GL060698

Jones, M., Sutton, E. K., Emmert, J. T., Siskind, D. E., & Drob, D. P. (2021). On the effects of mesospheric and lower thermospheric oxygen chemistry on the thermosphere and ionosphere semiannual oscillation. *Journal of Geophysical Research: Space Physics*, *126*, e2020JA028647. https://doi.org/10.1029/2020ja028647

Lei, J., Matsuo, T., Dou, X., Sutton, E., & Luan, X. (2012). Annual and semiannual variations of thermospheric density: EOF analysis of CHAMP and GRACE data. *Journal of Geophysical Research*, *117*, A01310. https://doi.org/10.1029/2011JA017324

Paetzold, H. K., & Zschörner, H. (1961). An annual and a semiannual variation of the upper air density. *Pure and Applied Geophysics*, *48*, 85–92. https://doi.org/10.1007/bf01992371

Paxton, L. J., Christensen, A. B., Humm, D. C., Ogorzalek, B. S., Pardoe, C. T., Morrison, D., et al. (1999). Global ultraviolet imager (GUVI): Measuring composition and energy inputs for the NASA thermosphere ionosphere mesosphere energetics and dynamics (TIMED) mission. *SPIEOptical Spectroscopic Techniques and Instrumentation for Atmospheric and Space Research III*. (Vol. *3756*, pp. 265–276).

Picone, J. M., Hedin, A. E., Drob, D. P., & Aikin, A. C. (2002). NRLMSISE-00 empirical model of the atmosphere: Statistical comparisons and scientific issues. *Journal of Geophysical Research*, *107*, A12. 1468. https://doi.org/10.1029/2002JA009430

Pilinski, M. D., & Crowley, G. (2015). Seasonal variability in global eddy diffusion and the effect on neutral density. *Journal of Geophysical Research: Space Physics*, *120*, 3097–3117. https://doi.org/10.1002/2015JA021084

Qian, L., Burns, A. G., Emery, B. A., Foster, B., Lu, G., Maute, A., et al. (2014). The NCAR TIE-GCM: A community model of the coupled thermosphere/ionosphere system. *American Geophysical monograph*. https://doi.org/10.1002/9781118704417.ch7

Qian, L., Burns, A. G., Solomon, S. C., & Wang, W. (2013). Annual and semiannual variation of the ionosphere. *Geophysical Research Letters*, *40*, 1928–1933. https://doi.org/10.1002/grl.50448

Qian, L., Burns, A. G., Wang, W., Solomon, S. C., & Zhang, Y. (2016). Longitudinal variations of thermospheric composition at the solstices. *Journal of Geophysical Research: Space Physics*, *121*, 6818–6829. https://doi.org/10.1002/2016JA022898

Qian, L., Burns, A. G., Wang, W., Solomon, S. C., Zhang, Y., & Hsu, V. (2016). Effects of the equatorial ionosphere anomaly on the interhemispheric circulation in the thermosphere. *Journal of Geophysical Research: Space Physics*, *121*, 2522–2530. https://doi.org/10.1002/2015JA022169

Qian, L., & Solomon, S. C. (2011). Thermospheric density: An overview of temporal and spatial variations. *Space Science Reviews*, *168*, 147–173. https://doi.org/10.1007/s11214-011-9810-z

Qian, L., Solomon, S. C., & Kane, T. J. (2009). Seasonal variation of thermospheric density and composition. *Journal of Geophysical Research*, *114*, A01312. https://doi.org/10.1029/2008JA013643

Qian, L., & Yue, J. (2017). Impact of the lower thermospheric winter-to-summer residual circulation on thermospheric composition. *Geophysical Research Letters*, *44*, 3971–3979. https://doi.org/10.1002/2017GL073361

Reigber, C., Balmino, G., Schwintzer, P., Biancale, R., Bode, A., Lemoine, J. M., et al. (2002). A high quality global gravity field model from CHAMP GPS tracking data and accelerometry (EIGEN-1S). *Geophysical Research Letters*, *29*(14), 37–41. https://doi.org/10.1029/2002GL015064

Richmond, A. D., Ridley, E. C., & Roble, R. G. (1992). A thermosphere/ionosphere general circulation model with coupled electrodynamics. *Geophysical Research Letters*, *19*, 601–604. https://doi.org/10.1029/92gl00401

Rishbeth, H., & Müller-Wodarg, I. C. F. (1999). Vertical circulation and thermospheric composition: A modelling study. *Annals of Geophysics*, *17*, 794–805. https://doi.org/10.1007/s00585-999-0794-x

Rishbeth, H., Müller-Wodarg, I. C. F., Zou, L., Fuller-Rowell, T. J., Millward, G. H., Moffett, R. J., et al. (2000). Annual and semiannual variations in the ionospheric F2-layer: II. Physical discussion. *Annals of Geophysics*, *18*, 945–956. https://doi.org/10.1007/s00585-000-0945-6

Roble, R. G., Ridley, E. C., Richmond, A. D., & Dickinson, R. E. (1988). A coupled thermosphere/ionosphere general circulation model. *Geophysical Research Letters*, *15*, 1325–1328. https://doi.org/10.1029/gl015i012p01325

Tapley, B. D., Bettadpur, S., Watkins, M., & Reigber, C. (2004). The gravity recovery and climate experiment: Mission overview and early results. *Geophysical Research Letters*, *31*(9), L09607. https://doi.org/10.1029/2004GL019920

Weimer, D. R., Mehta, P. M., Tobiska, W. K., Doornbos, E., Mlynczak, M. G., Drob, D. P., & Emmert, J. T. (2020). Improving neutral density predictions using exospheric temperatures calculated on a geodesic, polyhedral grid. *Space Weather*, *18*, e2019SW002355. https://doi.org/10.1029/2019SW002355

Wu, Q., Schreiner, W. S., Ho, S.-P., Liu, H.-L., & Qian, L. (2017). Observations and simulations of eddy diffusion and tidal effects on the semi-annual oscillation in the ionosphere. *Journal of Geophysical Research: Space Physics*, *122*. https://doi.org/10.1002/2017JA024341

Yamazaki, Y., & Richmond, A. D. (2013). A theory of ionospheric response to upward-propagating tides: Electrodynamic effects and tidal mixing effects. *Journal of Geophysical Research: Space Physics*, *118*, 5891–5905. https://doi.org/10.1002/jgra.50487

Yu, T., Ren, Z., Le, H., Wan, W., Wang, W., Cai, X., et al. (2020). Seasonal variation of O/N_2 on different pressure levels from GUVI limb measurements. *Journal of Geophysical Research: Space Physics*, *125*, e2020JA027844. https://doi.org/10.1029/2020ja027844

Yue, J., Jian, Y., Wang, W., Meier, R. R., Burns, A., Qian, L., et al. (2019). Annual and semiannual oscillations of thermospheric composition in TIMED/GUVI limb measurements. *Journal of Geophysical Research: Space Physics*, *124*. https://doi.org/10.1029/2019ja026544

Zeng, Z., Burns, A., Wang, W., Lei, J., Solomon, S., Syndergaard, S., et al. (2008). Ionospheric annual asymmetry observed by the COSMIC radio occultation measurements and simulated by the TIEGCM. *Journal of Geophysical Research*, *113*, A07305. https://doi.org/10.1029/2007JA012897

Zhang, S.-R., Holt, J. M., Van Eyken, A. P., Heinselman, C., & McCready, M. (2010). IPY observations of ionospheric yearly variations from high-to middle-latitude incoherent scatter radars. *Journal of Geophysical Research*, *115*(A3), A03303. https://doi.org/10.1029/2009ja014327

Zhang, S.-R., Holt, J. M., Van Eyken, A. P., McCready, M., Amory-Mazaudier, C., Fukao, S., & Sulzer, M. P. (2005). Ionospheric local model and climatology from long-term databases of multiple incoherent scatter radars. *Geophyical Research Letters*, *32*(20), 9481. https://doi.org/10.1029/2005gl023603

Zhang, Y., Paxton, L. J., Morrison, D., Wolven, B., Kil, H., Meng, C.-I., et al. (2004). O/N2 changes during 1-4 October 2002 storms: IMAGE SI-13 and TIMED/GUVI observations. *Journal of Geophysical Research*, *109*, A10308. https://doi.org/10.1029/2004JA010441